# Politecnico di Torino

# Porto Institutional Repository

[Article] Ultrafast relaxation of photoexcited carriers in semiconductor quantum wires: A Monte Carlo approach

(Article begins on next page)

# Ultrafast relaxation of photoexcited carriers in semiconductor quantum wires: A Monte Carlo approach

Lucio Rota

*Department of Physics, Clarendon Laboratory, University of Oxford, Parks Road, Oxford OX1 3PU, United Kingdom*

Fausto Rossi

*Fachbereich Physik und Zentrum für Materialwissenschaften, Philipps-Universität Marburg, Renthof 5, 35032 Marburg, Germany*

Paolo Lugli

*Dipartimento di Ingegneria Elettronica, Università di Roma "Tor Vergata," Via della Ricerca Scientifica, I-00133 Roma, Italy*

Elisa Molinari

*Dipartimento di Fisica, Università di Modena, Via Campi 213/A, I-41100 Modena, Italy*

A detailed analysis of the cooling and thermalization process for photogenerated carriers in semiconductor quantum wires is presented. The energy relaxation of the nonequilibrium carrier distribution is investigated for the "realistic" case of a rectangular multisubband quantum-wire structure. By means of a direct ensemble Monte Carlo simulation of both the carrier and the phonon dynamics, all the nonlinear phenomena relevant for the relaxation process, such as carrier-carrier interaction, hot-phonon effects, and degeneracy, are investigated. The results of these simulated experiments show a significant reduction of the carrier-relaxation process compared to the bulk case, which is mainly due to the reduced efficiency of carrier-carrier scattering; on the contrary, the role of hot-phonon effects and degeneracy seems to be not so different from that played in bulk semiconductors.

## I. INTRODUCTION

The strong push toward lower dimensionality of semiconductor structures has been motivated by the hope that the interactions experienced by charge carriers could be reduced in such systems. This in turn would result in higher mobilities, and faster semiconductor devices.[1] Such idealization is based on the fact that the phase-space available to carriers decreases with dimensionality, thus reducing the effectiveness of the scattering mechanisms.[2] Unfortunately, only semiconductor systems operating in the extreme quantum limit (low temperature, strong quantization) behave in this way.[2] However, in realistic low-dimensional structures, the number of occupied quantum states is so high and their separation so small that the transport properties do not differ significantly from systems of higher dimensionality.

From an experimental point of view, the most effective way to study the strength of the various scattering mechanisms and their dependence on dimensionality is through the time-resolved spectroscopical analysis of the cooling of photoexcited carriers.[3] The cooling process is mainly controlled by carrier-LO phonon and carrier-carrier (CC) interactions. By monitoring the time evolution of the carrier distribution functions, it is possible to extract relevant information on the scattering rates. The process is actually quite complicated. In fact, a hot-carrier population produced by optical excitation relaxes to its equilibrium state by dissipating energy to the lattice. In polar semiconductors this process occurs mostly through the emission of small wave-vector polar-optical phonons, at least as long as the carriers remain mainly in the Γ valley. If the excitation energy and the carrier density are sufficiently high, this phonon emission can drive the phonon population out of equilibrium. In turn, the hot-phonon population can approach its equilibrium distribution either decaying into large wave-vector acoustic phonons or being reabsorbed by the carrier system. Since the typical anharmonic-decay time of optical phonons is much longer than the electron-phonon scattering time, hot-phonon reabsorption is the dominant process in the early stages after optical excitation.[4] For relatively high carrier densities it is therefore necessary to study the *joint* evolution of the carrier and phonon distributions. In the high-density regime, two additional effects become important: *degeneracy*, which tends to reduce the carrier cooling rate when band-filling effects become relevant, and *carrier-carrier scattering*, which modifies the overall thermalization by spreading carriers over a large energy range and by exchanging energy and momentum between carriers in different bands. All these nonlinear phenomena are strictly interconnected, and they need to be considered together in order to understand the physical behavior of the system.

In quantum wires, hot-phonon degeneracy and screening effects could even be more important than in bulk system, since—due to the very limited size of these systems—all experiments and probably all future device applications will require relatively high carrier densities, which will result in a highly nonequilibrium phonon pop-

ulation. Some of these effects have been recently considered by several authors[5-14] within particular approximation schemes. Even though these results are often interesting and show some peculiar properties of one-dimensional (1D) systems, a complete picture for what concerns the carrier cooling and relaxation under highly nonequilibrium conditions is still missing.

In this paper, we will present a theoretical analysis of the ultrafast relaxation of photoexcited carriers in rectangular quantum wires (QWR).[15,16] This is based on a Monte Carlo (MC) solution of a coupled set of Boltzmann transport equations,[17,18] which results into a direct ensemble Monte Carlo (EMC) simulation of both the carrier and the phonon dynamics.

The paper is organized as follows: In Sec. II, the physical system and the theoretical approach are presented; in Sec. III, we will describe the Monte Carlo procedure for the solution of the set of Boltzmann transport equations; In Sec. IV, the results of our Monte Carlo simulations are discussed; Finally, in Sec. V we will draw our conclusions.

## II. PHYSICAL SYSTEM

The physical system we consider is a gas of photogenerated carriers confined in a quasi-one-dimensional semiconductor structure. The carriers interact with each other and with the various phonon modes of the semiconductor crystal.

Such a system is described by a total Hamiltonian **H** which, as usual, can be decomposed in a part **H**$_0$ which is treated "exactly," and a part **H**$_1$, which is treated within some approximation scheme. In particular, the term **H**$_0$ will be the sum of the two Hamiltonian **H**$_c$ and **H**$_p$, describing the noninteracting carriers and the phonon system, respectively, while **H**$_1$ can be expressed as the sum of a term **H**$_2$, describing the carrier-generation process induced by the external laser field, and the total scattering Hamiltonian **H**$_s$, describing the various interaction mechanisms, i.e., carrier-carrier, carrier-phonon, and phonon-phonon interaction. Let us now discuss the structure of all these contributions for the case of a semiconductor QWR.

### A. Free-carrier dynamics

By "free carriers," we refer to the gas of noninteracting carriers confined within the quasi-one-dimensional semiconductor structure. The quantum confinement, due to the different energy gap of the two semiconductor materials, e.g., GaAs and $Al_xGa_{1-x}As$, is usually described in terms of a confinement potential $V^c$, whose height is dictated by the valence- and conduction-band discontinuities.

As the energy region of interest is relatively close to the QWR band gap, we are allowed to describe the bulk band structure in terms of the usual effective-mass approximation. In addition, since the confinement potential $V^c$ is a slowly varying function on the scale of the lattice periodicity, we are allowed to work within the so-called "envelope-function approximation," i.e., the total wave function is given by the usual Bloch functions $U$ multiplied by a slowly varying part $\phi$, called envelope function.

By denoting with $x$ the QWR free direction, the confinement potential $V^c$ will be a function of the two confinement directions $y$ and $z$ only, i.e., the system is still translationally invariant (with the crystal periodicity) along the QWR direction. As a consequence, the $x$ component of the carrier wave vector **k** is still a "good" quantum number and the carrier wave function can be factorized in terms of a plane wave $\phi(x)$ along the free direction times an envelope function $\phi(y,z)$ over the normal plane.

As a result, the carriers within our QWR structure are described by the two-dimensional (2D) Schrödinger equation:

$$\left[ -\frac{\hbar^2}{2m^*} \left[ \frac{\partial^2}{\partial^2 y} + \frac{\partial^2}{\partial^2 z} \right] + V^c(y,z) \right] \phi_i(y,z) = \mathcal{E}_i \phi_i(y,z) \ ,$$

(1)

where $m^*$ denotes the bulk effective mass. Here, the set of eigenvalues $\mathcal{E}_i$ correspond to the different energy levels of the carriers induced by the confinement potential profile $V^c$; therefore, the explicit form of the band structure for a carrier in the QWR is

$$\mathcal{E}_{i,k_x} = \mathcal{E}_i + \frac{\hbar^2 k_x^2}{2m^*} \ .$$

(2)

The above expression shows that for each of the energy levels $\mathcal{E}_i$ (corresponding to the quantum confinement along both $y$ and $z$ directions), we have a 1D parabolic band, named "subband," characterized by the same bulk effective mass $m^*$.

Given the carrier band structure $\mathcal{E}_{i,k_x}$, the free-carrier Hamiltonian can be easily written within the standard second-quantization picture as

$$\mathbf{H}_c = \sum_{i,k_x} \mathcal{E}_{i,k_x} c_{i,k_x}^\dagger c_{i,k_x} \ ,$$

(3)

where $c_{i,k_x}^\dagger$ and $c_{i,k_x}$ are the two sets of creation and annihilation operators which, when applied to the state vector of the system, create and annihilate a carrier with $x$-wave-vector component $k_x$ within subband $i$, respectively.

Let us conclude this section by discussing the explicit form of the energy levels $\mathcal{E}_i$ and of the corresponding envelope functions $\phi_i$ for the particular QWR structures, we will consider in our Monte Carlo analysis. Such structures are those fabricated by chemical etching starting from multiple quantum well (QW) samples. Such a technique allows us to obtain a GaAs rectangular quantum wire confined in the (vertical) growth direction ($z$) by $Al_xGa_{1-x}As$ layers, and free standing along the transverse direction ($y$).[15]

The confinement potential $V^c$ corresponding to this QWR structure can be easily written as the sum of two square-well potential profiles, each of them depending on one of the two confinement coordinates:

$$V^c(y,z) = V^y(y) + V^z(z) ,\qquad(4)$$

with

$$V^y(y) = \begin{cases} 0, & -\dfrac{L_y}{2} < y < \dfrac{L_y}{2} \\[2mm] \infty & \text{otherwise} \end{cases}\qquad(5)$$

and

$$V^z(z) = \begin{cases} 0, & -\dfrac{L_z}{2} < z < \dfrac{L_z}{2} \\[2mm] V_0 & \text{otherwise.} \end{cases}\qquad(6)$$

Here, we have denoted with $L_y$ and $L_z$ the dimensions of the rectangular QWR and we have implicitly placed the origin of the $y,z$ coordinates at the center of the QWR cross section.

The particular form (4) of the potential profile leads to an additional factorization of the carrier dynamics, with respect to the two confinement directions: the envelope function $\phi$ is the product of two 1D envelope functions,

$$\phi_i(y,z) = \phi_{iy}^y(y)\phi_{iz}^z(z)\qquad(7)$$

and the corresponding energy levels are the sum of those of the two 1D problems,

$$\mathscr{E}_i \equiv \mathscr{E}_{i_y i_z} = \mathscr{E}_{i_y}^y + \mathscr{E}_{i_z}^z ,\qquad(8)$$

where $i_y$ and $i_z$ denote the quantum numbers corresponding to the two confinement directions $y$ and $z$, respectively.

From the above considerations, we see that solving the problem for such a QWR structure reduces to solving that of two QW structures, i.e., in order to obtain the envelope functions $\phi_i$ and the corresponding energy levels $\mathscr{E}_i$, for each of the two confinement directions, we need to solve the corresponding Schrödinger problems. The solutions corresponding to the square-well potential profiles $V^y$ and $V^z$ given in Eqs. (5) and (6) are shown in Fig. 1 together with the contour plot of the two-dimensional wave function $\phi_i(y,z)$ and a schematic representation of the ten energy levels confined in the wire.

We stress, however, that in general the above factorization along the two confinement directions is not possible. This is true not only for wires with complex profiles — such as, e.g., $V$-shaped wires[19]—, but also for QWR with simple shapes, as the case of a rectangular GaAs QWR fully embedded in $Al_xGa_{1-x}As$. In such a structure, the confinement potential $V^c$ can be taken to be zero within the QWR and equal to a constant value $V_0$ outside. This potential cannot be expressed as $V^c$ in Eq. (4). Nevertheless, also in this case such factorization has been used as an approximation to the exact solution; in general, this is quite good for the lowest-energy levels in "wide" QWR structures, but it becomes very questionable for the energy levels close to the top of the potential barrier.
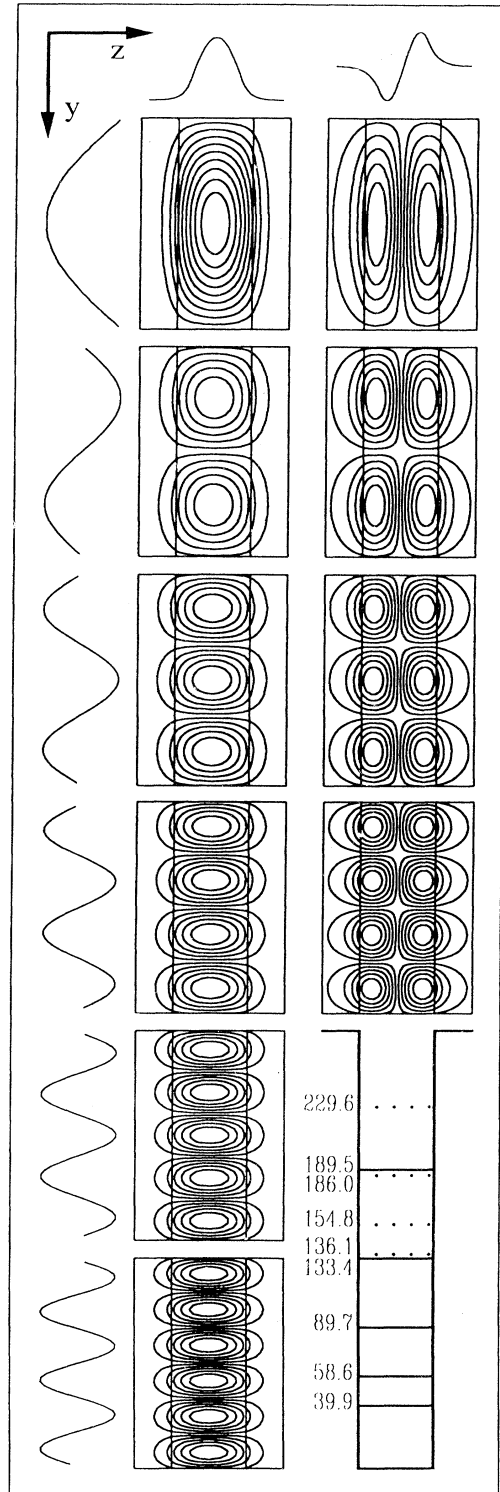


FIG. 1. Contour plots of the electron wave functions corresponding to the ten energy levels confined in the QWR. The factorization of the solutions along the $y$ and $z$ directions is shown too. In the lower right corner, the values and the relative position of the energy levels are shown, solid and dotted lines correspond, respectively, to energy levels with $i_z = 1$ and 2.

## B. Free-phonon dynamics

Let us now come to the analysis of the free-phonon properties of our QWR structure. By "free phonons" we refer to harmonic lattice vibrations; the role of the nonharmonic terms (phonon-phonon interactions) will be discussed in Sec. II C 3.

It is well known that, moving from bulk systems to heterostructures, the partial loss of spatial symmetry leads to important modifications in the vibrational behavior of the system. The extensive analysis performed during the last decade on QW structures has shown that—similarly to carriers—optical phonons may be confined in one of the constituent materials (for reviews see, e.g., Refs. 20–22). Moreover, in polar semiconductor heterostructures interface phonon modes exist, which give rise to potentials with maxima on the interfaces.[20–24]

Several approaches exist for the theoretical analysis of optical-phonon spectra in low-dimensional systems, based on either microscopic or macroscopic models.[20–22] In the following, we will employ the dielectric continuum model, which has been shown to be sufficiently reliable for the study of the electron-phonon scattering rates in QW's and QWR's.[22–26]

From the analysis of phonon properties in 2D systems,[22,25,27,28] we know that the following "sum rule" holds: the total effect of confined and interface phonons on the electron-phonon scattering rates is very close to that of bulk phonons of the well (barrier) material in the thick (thin) limit, and always falls between those extrema for intermediate well thicknesses. For a 100-Å GaAs QW embedded in $Al_xGa_{1-x}As$, the total electron-phonon scattering rate is very well approximated by considering bulk GaAs phonons. The same arguments holding for 2D systems are expected to hold, in general, also for wires.[22,25,27,28] The validity and good accuracy of this sum rule in our case will be shown in Sec. II D 1.

As previously mentioned, we are interested in GaAs rectangular quantum wires confined in the (vertical) growth direction ($z$) by $Al_xGa_{1-x}As$ layers, and free standing along the transverse direction ($y$). The typical QWR dimensions are of about 300 and 100 Å in the $y$ and $z$ directions, respectively.

On the basis of these considerations, we choose the following phonon model: We will consider bulk-phonon modes along the $x$ and $z$ direction and only confined modes along the $y$ direction. The latter approximation follows from the fact that along $y$, the wire is so large that the effect of interface modes is negligible. The results of this model are equivalent to those obtained by a full treatment of the phonon spectrum, as we have verified numerically; the advantage of the model is that it is simpler and, therefore, allows a better understanding of the intersubband carrier and hot-phonon dynamics.

Our phonons are then characterized by continuous wave vectors $q_x$ and $q_z$ in the two free directions and by the index $\nu$ along the $y$ direction. In order to simplify the notation, and for coherence with the free-carrier indices, we introduce an index $\lambda \rightarrow \nu, q_z$. By denoting with $b^\dagger_{\lambda, q_x}$ and $b_{\lambda, q_x}$ the set of phonon creation and annihilation operators, we can then write the free-phonon Hamiltoni-

an as

$$\mathbf{H}_p = \sum_{\lambda, q_x} \hbar \omega_{\lambda, q_x} b^\dagger_{\lambda, q_x} b_{\lambda, q_x} \ , \tag{9}$$

where $\omega_{\lambda, q_x}$ denotes the set of phonon dispersions.

### C. Interacting dynamics

As discussed at the beginning of Sec. II, our total Hamiltonian is split into a part $\mathbf{H}_0$ that we are able to solve exactly plus an additional part $\mathbf{H}_1$ that will be treated within some approximation scheme. Let us now discuss the explicit terms of this perturbation Hamiltonian.

#### 1. Carrier photogeneration

The Hamiltonian $\mathbf{H}_g$ previously introduced corresponds to the light-matter interaction, i.e., the interaction of the external laser field with our QWR semiconductor. It describes the creation and recombination processes of electron-hole pairs induced by the external light field. Therefore, its explicit form involves, in additional to the creation and annihilation operators for electrons, the corresponding ones for holes. Here, we are not interested in discussing the details of the photogeneration process, which can be found in Refs. 29–31. We only stress that the carrier generation rates commonly used in EMC simulations can be derived from $\mathbf{H}_g$ within Fermi's golden rule approximation. Therefore, we will simply describe the carrier generation process in terms of a rate $G_{i, k_x}(t)$, defined as the average number of generated carriers in state $i, k_x$ per unit time. In particular, in our simulated experiments, we will assume a laser intensity proportional to $\mathrm{sech}(t / \tau_{l_p} \beta)$, where $\beta = 1.762$ is the autocorrelation of the laser pulse. Due to the time-energy uncertainty relation, the generation rate will exhibit an energy broadening around the energy-conserving vertical transition given by the Fourier transform of the laser intensity.

#### 2. Carrier-phonon interaction

Let us now discuss the explicit form of the carrier-phonon Hamiltonian. In terms of the previously defined electron and phonon creation and annihilation operators, it can be written as

$$
\mathbf{H}^{cp} = \sum_{i, k_x, \lambda, q_x, m, k_x'} \alpha^{cp}_{m, k_x'; \lambda, q_x; i, k_x} c^\dagger_{m, k_x'} b_{\lambda, q_x} c_{i, k_x}
$$
$$
+ \sum_{i, k_x, \lambda, q_x, m, k_x'} \alpha^{cp}_{m, k_x'; \lambda, -q_x; i, k_x} c^\dagger_{m, k_x'} b^\dagger_{\lambda, -q_x} c_{i, k_x} \ ,
$$

$$\tag{10}$$

where the $\alpha$'s denote the carrier-phonon form factors:

$$\alpha^{cp}_{m, k_x'; \lambda, q_x; i, k_x} = \int d\mathbf{r} \Phi^*_{m, k_x'}(\mathbf{r}) \Psi_{\lambda, q_x}(\mathbf{r}) \Phi_{i, k_x}(\mathbf{r}) \ , \tag{11}$$

where $\Psi_{\lambda, q_x}(\mathbf{r})$ is the electrostatic phonon potential. The second quantization picture provides a direct interpretation of the above Hamiltonian: The first term on the right-hand side of Eq. (10) describes an electron transition from state $i, k_x$ to state $m, k_x'$ (one electron is de-

stroyed in the initial state and an electron is created in the final one) induced by the emission of a phonon of wave vector $q_x$ and mode $\lambda$, while the second term describes the same electron transition induced by the absorption of a phonon of wave vector $-q_x$ and mode $\lambda$.

### 3. Phonon-phonon interaction

The free-phonon Hamiltonian (9) introduced in Sec. II B, which describes a system of noninteracting phonons, by definition accounts only for the harmonic part of the lattice potential. However, nonharmonic contributions of the interatomic potential can play an important role in determining the lattice dynamics in highly excited systems,[32] as they are responsible for the decay of optical phonons into phonons of lower frequency. In our picture, these nonharmonic contributions can be described in terms of a phonon-phonon interaction which induces, in general, transitions between free-phonon states. We will not discuss in this paper the explicit form of the phonon-phonon Hamiltonian responsible for such decay. However, as we will discuss in Sec. II D, this effect is introduced in our kinetic description in terms of a relaxation-time approximation, i.e., through a phenomenological decay time of our phonon population. This approximation is quite good on the time scale that we are interested in, where the phonon decay affects only slightly the nonequilibrium phonon distribution.

### 4. Carrier-carrier interaction

In terms of the electron creation and annihilation operators introduced in Sec. II A, the carrier-carrier interaction Hamiltonian can be written as

$$\mathbf{H}^{cc} = \sum_{i,k_1;j,k_2;m,k_1';n,k_2'} \alpha^{cc}_{i,k_1;j,k_2 \to m,k_1';n,k_2'}$$

$$\times c^\dagger_{m,k_1'} c^\dagger_{n,k_2'} c_{i,k_1} c_{j,k_2} , \qquad (12)$$

where, in order to simplify the notation, we have dropped the index $x$ (we will keep this notation in all parts concerning the CC interaction), while the $\alpha^{cc}$'s are the form-factor coefficients for carrier-carrier interaction:

$$\alpha^{cc}_{i,k_1;j,k_2 \to m,k_1';n,k_2'}$$

$$= \int d\mathbf{r}_1 \int d\mathbf{r}_2 \Phi^*_{m,k_1'}(\mathbf{r}_2) \Phi^*_{n,k_2'}(\mathbf{r}_1) \frac{e^2}{4\pi\varepsilon_s |\mathbf{r}_2 - \mathbf{r}_1|}$$

$$\times \Phi_{i,k_1}(\mathbf{r}_2) \Phi_{j,k_2}(\mathbf{r}_1) . \qquad (13)$$

Here, $e$ and $\varepsilon_s$ denote the electron charge and the static dielectric constant, respectively.

As usual, the second quantization picture allows a direct physical interpretation of Eq. (12): the Hamiltonian describes a generic transition from the initial state $i,k_1;j,k_2$ to the final state $m,k_1';n,k_2'$ in terms of the destruction of two electrons in states $i,k_1$ and $j,k_2$, and the creation of other two electrons in states $m,k_1'$ and $n,k_2'$. We stress that, in contrast to the case of a bulk semiconductor, the above carrier-carrier Hamiltonian does not

reflect full momentum conservation, which, in general, does not hold for a nonhomogeneous system as a QWR structure; The explicit calculation of the factor $\alpha^{cc}$ shows that of course we still have momentum conservation along the free $(x)$ QWR direction.

### D. Set of kinetic equations

As a starting point, let us introduce the set of kinetic variables, which describe the electron-phonon system within our structure. The carriers are described in terms of the various distribution functions corresponding to the different QWR subbands,

$$f_{i,k_x} = \langle c^\dagger_{i,k_x} c_{i,k_x} \rangle , \qquad (14)$$

while the phonon system is described in terms of the various occupation functions corresponding to the different phonon modes,

$$n_{\lambda,q_x} = \langle a^\dagger_{\lambda,q_x} a_{\lambda,q_x} \rangle . \qquad (15)$$

Therefore, the quantity $f_{i,k_x}$ denotes the average occupating number of carriers with wave vector $k_x$ in the subband $i$, while $n_{\lambda,q_x}$ denotes the average occupation number of phonons of mode $\lambda$ and wave vector $q_x$.

Given the above set of kinetic variables, let us now introduce the corresponding set of kinetic equations. The physical process of interest can be qualitatively summarized as follows. In the presence of laser photoexcitation, when electrons are injected in the system with sufficiently high energy, they relax towards equilibrium mainly through the emission of polar-optical phonons. In turn, this rapid emission of phonons in a limited region of the total phase space increases the phonon occupancy $n_{\lambda,q_x}$ in such region, thus creating a nonequilibrium phonon distribution. At this point the phonon distribution can relax toward equilibrium through two different channels. Small wave-vector LO phonons can decay into acoustic phonons through anharmonic interaction, or they can be reabsorbed by the carrier distribution. As the decay time into acoustic phonons is relatively long—7 ps in GaAs at low temperature[4,32]—both the electron and phonon systems relax jointly towards equilibrium within few picoseconds.

Within the standard semiclassical (Boltzmann) transport theory, this process can be analyzed in terms of a coupled system of Boltzmann-like equations describing the time evolution of the above set of kinetic variables. Here, we will not discuss the details of the derivation, which is similar to that contained in Ref. 29 for the case of a bulk semiconductor.

The resulting system of kinetic equations can be schematically written as

$$\frac{d}{dt} f_{i,k_x} = \frac{d}{dt} f_{i,k_x}\bigg|_{cc} + \frac{d}{dt} f_{i,k_x}\bigg|_{cp} + G_{i,k_x}(t) ,$$

$$\frac{d}{dt} n_{\lambda,q_x} = \frac{d}{dt} n_{\lambda,q_x}\bigg|_{cp} + \frac{d}{dt} n_{\lambda,q_x}\bigg|_{pp} , \qquad (16)$$

where $G_{i,k_x}$ denotes the generation rate of carriers (with momentum $k_x$ within subband $i$), due to the external laser field. The time evolution of the carrier distribution is due to carrier-carrier and carrier-phonon interaction (plus the contribution due to carrier photogeneration), while that of the phonon occupation number is due to carrier-phonon and phonon-phonon interaction. We neglect here the carrier recombination rate, which is too low to affect the distribution function on the picosecond time scale that we are interested in.

The terms on the right-hand side of Eq. (16) have the following structure of rate equations:

$$\frac{d}{dt}f_{i,k_x}\bigg|_{cc} = \sum_{m,k_x'} [P^{cc}_{m,k_x';i,k_x}f_{m,k_x'} - P^{cc}_{i,k_x;m,k_x'}f_{i,k_x}] , \quad (17)$$

$$\frac{d}{dt}f_{i,k_x}\bigg|_{cp} = \sum_{m,k_x'} [P^{cp,em}_{m,k_x';i,k_x}f_{m,k_x'} - P^{cp,em}_{i,k_x;m,k_x'}f_{i,k_x}]$$

$$+ \sum_{m,k_x'} [P^{cp,ab}_{m,k_x';i,k_x}f_{m,k_x'} - P^{cp,ab}_{i,k_x;m,k_x'}f_{i,k_x}] , \quad (18)$$

$$\frac{d}{dt}n_{\lambda,q_x}\bigg|_{cp} = \mathcal{P}^{cp,em}_{\lambda,q_x}(n_{\lambda,q_x}+1) - \mathcal{P}^{cp,ab}_{\lambda,q_x}n_{\lambda,q_x} , \quad (19)$$

$$\frac{d}{dt}n_{\lambda,q_x}\bigg|_{pp} = \frac{N^B_{\lambda,q_x} - n_{\lambda,q_x}}{\tau_{pp}} , \quad (20)$$

where $P^{cc}_{i,k_x;m,k_x'}$, $P^{cp,em}_{i,k_x;m,k_x'}$ and $P^{cp,ab}_{i,k_x;m,k_x'}$ are, respectively, the carrier-carrier, carrier-phonon emission, and absorption scattering rates for a transition from state $i,k_x$ to state $m,k_x'$, while $\mathcal{P}^{cp,em}_{\lambda,q_x}$ and $\mathcal{P}^{cp,ab}_{\lambda,q_x}$ denote the rates of change of the phonon population, due to phonon emission and absorption, respectively. As we will discuss in Sec. II C 3, the effect of phonon-phonon interaction results in a hot-phonon lifetime $\tau_{pp}$, which provides a "thermalization" of the phonon population towards the equilibrium Bose distribution $N^B_{\lambda,q_x}$.

For both the contributions to the time evolution of $f_{i,k_x}$ [Eqs. (17) and (18)], it is easy to recognize the typical structure of the "Boltzmann collision term," i.e., an in-scattering plus an out-scattering contribution. On the contrary, the structure of the contributions to $n_{\lambda,q_x}$ [Eqs. (19) and (20)] is different; this is due to the fact that, while the carrier collision terms need to preserve the total number of particles, this is not true for the case of phonons.

The above system of coupled equations will be solved in terms of a joint EMC simulation of both the carrier and phonon dynamics, which will be described in the following section.

Within our semiclassical approach, the explicit form of the above scattering rates is

$$P^{cc}_{i,k_1;m,k_1'} = \frac{2\pi}{\hbar} \sum_{j,k_2,n,k_2'} |\alpha^{cc}_{i,k_1;j,k_2 \to m,k_1',n,k_2'}|^2 f_{j,k_2}(1-f_{n,k_2'})(1-f_{m,k_1'})\delta(\mathcal{E}_{m,k_1'}+\mathcal{E}_{n,k_2'}-\mathcal{E}_{i,k_1}-\mathcal{E}_{j,k_2}) , \quad (21)$$

$$P^{cp,em}_{i,k_x;m,k_x'} = \frac{2\pi}{\hbar} \sum_{\lambda,q_x} |\alpha^{cp}_{m,k_x';\lambda,-q_x;i,k_x}|^2 (n_{\lambda,q_x}+1)(1-f_{m,k_x'})\delta(\mathcal{E}_{m,k_x'}-\mathcal{E}_{i,k_x}+\hbar\omega_{\lambda,q_x}) , \quad (22)$$

$$P^{cp,ab}_{i,k_x;m,k_x'} = \frac{2\pi}{\hbar} \sum_{\lambda,q_x} |\alpha^{cp}_{m,k_x';\lambda,q_x;i,k_x}|^2 n_{\lambda,q_x}(1-f_{m,k_x'})\delta(\mathcal{E}_{m,k_x'}-\mathcal{E}_{i,k_x}-\hbar\omega_{\lambda,q_x}) , \quad (23)$$

$$\mathcal{P}^{cp,em}_{\lambda,q_x} = \frac{2\pi}{\hbar} \sum_{i,k_x,m,k_x'} |\alpha^{cp}_{m,k_x';\lambda,-q_x;i,k_x}|^2 f_{i,k_x}(1-f_{m,k_x'})\delta(\mathcal{E}_{m,k_x'}-\mathcal{E}_{i,k_x}+\hbar\omega_{\lambda,q_x}) , \quad (24)$$

$$\mathcal{P}^{cp,ab}_{\lambda,q_x} = \frac{2\pi}{\hbar} \sum_{i,k_x,m,k_x'} |\alpha^{cp}_{m,k_x';\lambda,q_x;i,k_x}|^2 f_{i,k_x}(1-f_{m,k_x'})\delta(\mathcal{E}_{m,k_x'}-\mathcal{E}_{i,k_x}-\hbar\omega_{\lambda,q_x}) . \quad (25)$$

Here, the $\alpha$'s are the various form factors introduced in the previous sections. All the above scattering rates exhibit the typical structure obtained from Fermi's golden rule, i.e., they are proportional to the square of the form-factor coefficient $\alpha$ and they contain the Dirac $\delta$ function of energy conservation. However, they provide additional information on the many-body nature of our carrier-phonon system: they automatically reflect the Pauli exclusion principle in the scattering process, i.e., any scattering rate results to be proportional to the phase-space filling factor $1-f$ of the final state. Let us now discuss the explicit structure of these scattering rates for our particular QWR semiconductor.

### 1. Carrier-phonon scattering rate

We start by evaluating the carrier-phonon scattering rate. Due to the factorization of both the electronic wave functions and the phonon potential, the form factors can be factorized too:

$$\alpha^{ab}_{em}(k',k,\pm q) = g_q \int dx\, \phi^*_{k_x'}(x)\psi_{\pm q_x}(x)\phi_{k_x}(x) \int dy \int dz\, \phi^*_m(y,z)\psi_\lambda(y,z)\phi_i(y,z)$$

$$= g_q \alpha^{cP}(i,m,\lambda)\delta(k_x \pm q_x - k_x') ,$$

where $\psi_{q_x}(x)$ and $\psi_\lambda(y,z)$ are the phonon potential, respectively, in the free direction and in the normal plane, while $g_q = e^2\hbar\omega_0/2V[q_x^2 + (\pi v/L_y)^2 + q_x^2](1/\varepsilon_\infty - 1/\varepsilon_0)$ contains the normalization coefficient of the electrostatic phonon potential.

We assume for the moment that the system is not degenerate so that $f_{m,k_x'} = 0$: in this way, we are overestimating the value of the scattering rate, but this will be corrected inside the MC procedure by means of a rejection technique. By introducing the full index dependence of the phonon modes (i.e., $\lambda \to v, q_z$), we can then write the total scattering rate as

$$\Gamma_{\text{em}}^{\text{ab}}(i,k_x) = \frac{2\pi}{\hbar}\frac{e^2\hbar\omega_0}{2V}\left[\frac{1}{\varepsilon_\infty} - \frac{1}{\varepsilon_0}\right]\sum_m \frac{L_x}{2\pi}\int dk_x' \sum_{q_x,v,q_z}\frac{1}{q_x^2+q_v^2+q_z^2}\delta(k_x \pm q_x - k_x')$$

$$\times |\alpha^{\text{cp}}(i,m,v,q_z)|^2 \begin{bmatrix} n_q \\ n_q+1 \end{bmatrix}\delta[\mathcal{E}_m(k_x') - \mathcal{E}_i(k_x) \mp \hbar\omega_0] \; ,$$

where we have written the sum over the final states as a sum over the possible subbands and an integral over $k_x$. The integrals over $q_x$ and $k_x$ are eliminated using the $\delta$ function of momentum and energy conservation, and the total scattering rate is given by

$$\Gamma_{\text{em}}^{\text{ab}}(i,k_x) = \frac{e^2\hbar\omega_0 m^*}{4\pi L_y \hbar^3}\left[\frac{1}{\varepsilon_\infty} - \frac{1}{\varepsilon_0}\right]\sum_m \sum_v \int_{q_z}dq_z\left[\frac{1}{k_{x,f}'(q_{x,f}^2+q_v^2+q_z^2)} + \frac{1}{k_{x,b}'(q_{x,b}^2+q_v^2+q_z^2)}\right]$$

$$\times |\alpha^{\text{cp}}(i,m,v,q_z)|^2 \begin{bmatrix} n_q \\ n_q+1 \end{bmatrix} \; , \tag{26}$$

where $k_{x,f}' = \sqrt{k_x + (2m^*/\hbar^2)(\mathcal{E}_i - \mathcal{E}_m \pm \hbar\omega_0)}$, $k_{x,b}' = -\sqrt{k_x + (2m^*/\hbar^2)(\mathcal{E}_i - \mathcal{E}_m \pm \hbar\omega_0)}$, and $q_{x,f} = k_x - k_{x,f}'$, $q_{x,b} = k_x - k_{x,b}'$ correspond to the only two possible solutions of the energy-conserving $\delta$ function, which are usually referred to as forward and backward scattering. The scattering rate is shown in Fig. 2 (solid line) and compared with that obtained from the dielectric continuum model[12,25] in which the contribution due to confined and interface phonons is accounted for separately (dashed and dotted line, respectively). As we can see, the total value of this more sophisticated model (dash-dotted line) is in excellent agreement with our simplified model. This confirms the validity of our model and of the "sum rule" for quantum wires.

### 2. Carrier-carrier scattering rate

Let us now evaluate the scattering rate for the two particle Coulomb interaction. By using the explicit form of the electron wave functions, the CC form factor for the case of a bare Coulomb interaction (no screening) can be written as[33]

$$\alpha_{i,k_1;j,k_2 \to m,k_1';n,k_2'}^{\text{cc}} = \frac{e^2}{4\pi\epsilon_s}\int dz \int dy \int dz' \int dy' \phi_i(y,z)\phi_j(y',z')\phi_m^*(y,z)\phi_n^*(y',z')$$

$$\times \frac{1}{L^2}\int dx \int dx' \frac{e^{-i(k_1 x + k_2 x')}e^{i(k_1'x + k_2'x')}}{\sqrt{(x-x')^2+(y-y')^2+(z-z')^2}}$$

$$= \frac{e^2}{2\pi\epsilon_s L}\int dz \int dy \int dz' \int dy' \phi_i(y,z)\phi_j(y',z')\phi_m^*(y,z)\phi_n^*(y',z')$$

$$\times \delta(k_1+k_2-k_1'-k_2')K_0[|q|\sqrt{(y-y')^2+(z-z')^2}] \; , \tag{27}$$

where $K_0$ is the zero integer-order Bessel function. We will denote this quantity with $(e^2/2\pi\epsilon_s L)\times\gamma^{\text{cc}}(q)\delta(k_1+k_2-k_1'-k_2')$. One intrasubband form factor and two intersubband ones are shown in Fig. 3(a): we can see how the intrasubband term (solid line) for two electrons in the first two subbands is almost three orders of magnitude higher than the intersubband ones (dashed line) representing a transition for an electron jumping from subband 1 to 3, while the partner one stays in 3, and is even much larger than that for a transition from 1 to 5 (dotted line). This makes clear that the intrasubband interaction will be the dominant one. However, as we will see from our results, the actual difference is not that large, because the final density of states can favor

an intersubband scattering, in particular, for high-energy electrons. Moreover, we can notice that the intrasubband form factor is peaked only at small values of $q$ (notice that the graph is in log-log scale), while the intersubband term is almost $q$ independent over a large range of $q$'s. Starting from Eq. (21), we can now compute the expression for the scattering rate. Also in this case, we assume that the occupancy of the final states is negligible, i.e., $f_{m,k_1'} = 0$ and $f_{n,k_2'} = 0$ (this will be "corrected" within the simulation by employing a corresponding rejection technique as discussed in the next section). By summing over all possible final states, we obtain
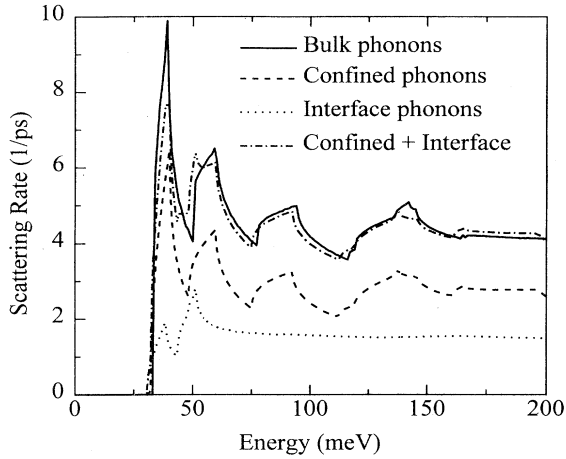
FIG. 2. Carrier-phonon scattering rates for confined and interface phonon modes and comparison between the sum of these modes and the bulk-phonon model used in the present work.

$$P_i^{cc}(k_1) = \frac{2\pi}{\hbar} \frac{e^4}{4\pi^2 \epsilon_s^2 L^2}$$

$$\times \sum_{j,k_2} \sum_m \sum_{n,k_2'} f_{j,k_2} \gamma^{cc}(q)^2$$

$$\times \delta[\mathcal{E}_m(k_1') + \mathcal{E}_n(k_2')$$

$$- \mathcal{E}_i(k_1) - \mathcal{E}_j(k_2)] , \qquad (28)$$

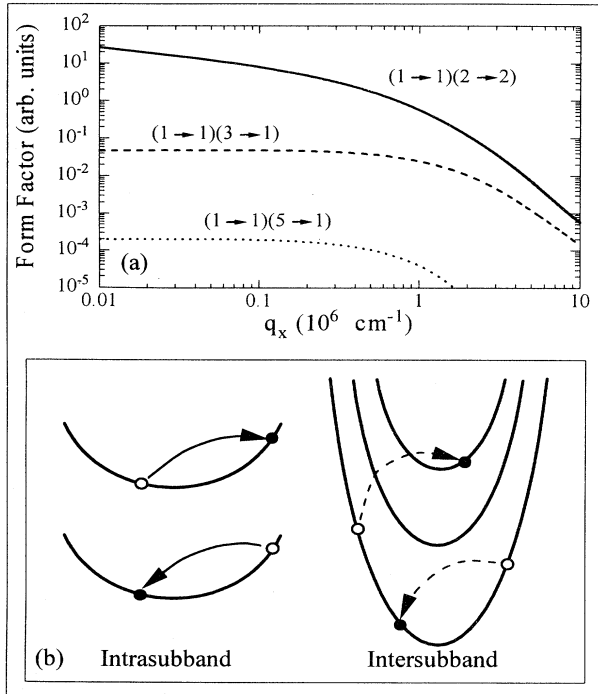where the sum over $k_1'$ has been eliminated using momen-



FIG. 3. Matrix elements for the carrier-carrier interaction (a) and schematic representation of the intrasubband and intersubband scattering (b).

tum conservation. The sum over $k_2'$ can be transformed into an integral; in terms of the relative wave vectors $g = k_2 - k_1$, $g' = k_2' - k_1'$ we can then write

$$P_i^{cc}(k_1) = \frac{e^4}{2\pi \epsilon_s^2 \hbar L^2}$$

$$\times \sum_{j,k_2} \sum_{m,n} f_{j,k_2} \frac{L}{2\pi} \frac{1}{2}$$

$$\times \int dg' \gamma^{cc}(q)^2 \delta[\mathcal{E}_m(k_1') + \mathcal{E}_n(k_2')$$

$$- \mathcal{E}_i(k_1) - \mathcal{E}_j(k_2)] ,$$

$$(29)$$

where the factor $\frac{1}{2}$ in front of the integral accounts for the fact that the density of states is doubled in going from the $k$ to the $g$ space. By writing explicitly the energy-conserving $\delta$ function, we finally have

$$P_i^{cc}(k_1) = \frac{e^4 m^*}{4\pi^2 \epsilon_s^2 \hbar^3 L} \sum_{j,k_2} \sum_{m,n} f_{j,k_2} \frac{1}{k_2 - k_1}$$

$$\times [\gamma^{cc}(q_+)^2 + \gamma^{cc}(q_-)^2] ,$$

$$(30)$$

where $q_+$ and $q_-$ are the only possible wave vectors exchanged in the interaction:

$$q_\pm = \frac{1}{2}(k_2 - k_1) \pm \left[ \frac{1}{4}(k_2 - k_1)^2 + \frac{m^* \Delta_{ijmn}}{\hbar^2} \right]^{1/2} , \qquad (31)$$

where $\Delta_{ijmn} = \mathcal{E}_i + \mathcal{E}_j - \mathcal{E}_m - \mathcal{E}_n$. Equation (31) shows that after the scattering, there are only two possible final states. Moreover, if $\Delta_{ijmn} = 0$ the solutions reduce to $q_+ = 0$ and $q_- = k_2 - k_1$. The first solution does not change the final states and is irrelevant to the scattering process. The second, as shown on the left-hand side of Fig. 3(b), corresponds to the exchange of momentum between the two particles. Even this process (usually referred to as intrasubband scattering) is irrelevant if both particles belong to the same subband, because they are indistinguishable and the initial and final state of the pair is then the same.[34] We shall then refer to intrasubband scattering as the interaction of two electrons that lie in different subbands, as long as they remain in their respective subbands after the scattering process. It is interesting to notice that in this case a creation of a new state in $k$ space never occurs, i.e., the CC scattering alone does not modify the total electron distribution function, leading only to an energy redistribution between different subbands. The only scattering that generates new $k$ states and, therefore, momentum relaxation, occurs when $\Delta_{ijmn}$ is different from zero, i.e., when at least one of the two particles changes subband. In this case, the energy difference between the initial and final subbands enters into the conservation law and allows the creation of two completely new states. A possible intersubband transition is sketched in the right-hand side of Fig. 3(b).

We must stress that these properties of the CC interaction in 1D systems follow from the use of the traditional semiclassical transport theory, where the interaction is

described in terms of binary collisions within a single-particle picture. If we make use of a full many-body simulation,[35] the restrictions on energy and momentum conservation disappear because energy and momentum can be redistributed over all the carriers through the long range of the interaction. Nevertheless the effect of the real intrasubband many-body interaction is very weak and has a significant effect only on a time scale of hundreds of picoseconds,[35] while, as we will see in our results, the intersubband binary scattering is already

effective on a subpicosecond time scale.

The carrier-carrier interaction is actually screened by all the carriers in the system: the screened scattering rate can be simply computed using the screened potential instead of the bare one; the matrix element can then be written in a slightly different form as[33]

$$\alpha^{cc}_{i,k_1;j,k_2 \to m,k'_1;n,k'_2} = \langle \phi^*_m(y,z) | V^{cc}_{j,n} | \phi_i(y,z) \rangle \ , \tag{32}$$

where

$$V^{cc}_{j,n} = \frac{e^2}{4\pi\epsilon_s L} \int dz' \int dy' \phi_j(y',z')\phi^*_n(y',z') \int dx' \frac{e^{-i(k_1 x + k_2 x')} e^{i(k'_1 x + k'_2 x')}}{\sqrt{(x-x')^2+(y-y')^2+(z-z')^2}} \ , \tag{33}$$

is the potential representing the interaction with a particle in subband $j$ that scatters in subband $n$. Within this formalism, the screened interaction can be written as

$$W^{cc}_{i,m} = \sum_{j,n} \varepsilon^{-1}_{i,m}(q,\omega) V^{cc}_{j,n} \ , \tag{34}$$

where $W^{cc}_{i,m}$ is the screened potential and $\varepsilon^{-1}_{i,m}(q,\omega)$ is the inverse of the dielectric function of the system. For a quantum wire, within the random-phase approximation (RPA), which has been proven to be quite accurate for such 1D systems,[7,8] the dielectric function is given by[33]

$$\varepsilon^{i,m}_{j,n}(q,\omega) = \delta_{i,m}\delta_{j,n} - L^{i,m}(q,\omega)\chi^{i,m}_{j,n}(q,\omega) \ , \tag{35}$$

where

$$\chi^{i,m}_{j,n}(q,\omega) = \frac{e^2}{\pi\epsilon_0 L} \int dy \int dy' \int dz \int dz' \phi_i(y,z)\phi_j(y',z')\phi^*_m(y,z)\phi^*_n(y',z') K_0[|q|\sqrt{(y-y')^2+(z-z')^2}] \ , \tag{36}$$

$$L^{i,m}(q,\omega) = \sum_k \frac{f[E_i(k+q)]-f(E_m(k))}{E_i(k+q)-E_m(k)-\hbar\omega+i\hbar\alpha} \ . \tag{37}$$

An exact treatment of the screening in the Monte Carlo simulation is for the moment computationally not feasible. The distribution function changes very quickly during and after the laser excitation, and we would need to compute the dielectric matrix for each value of $q$ and $\omega$ and to invert it at every time step. We then use the static approximation ($\omega=0$) and a simplified approach for the inversion of the matrix. It is well known that the static limit approximation of the RPA is not completely accurate, nevertheless recent ultrafast experiments[36] have shown that the error in this approach is not very large and limited to a time region of 100–200 fs during the laser excitation. As previously seen, the intrasubband matrix elements are much bigger than the intersubband ones. Therefore, the latter ones can be neglected and the dielectric matrix reduces to a 2D matrix, which can be written as[37]

$$\varepsilon_{i,j}(q,\omega) = \begin{vmatrix} 1-L^2\chi_{11} & -L^2\chi_{21} & -L^3\chi_{31} & \cdots \\ -L^1\chi_{12} & 1-L^2\chi_{22} & -L^3\chi_{32} & \cdots \\ -L^1\chi_{13} & -L^2\chi_{23} & 1-L^3\chi_{33} & \cdots \\ \vdots & \vdots & \vdots & \ddots \end{vmatrix} \ . \tag{38}$$

The screened matrix element can be simply obtained dividing the unscreened one by the determinant of this matrix (see Appendix A for the derivation). Therefore, the screened scattering rate is still given by Eqs. (12) and (32), with the following substitution:

$$W^{cc}_{i,m} \to \frac{V^{cc}_{j,n}}{|\varepsilon_{i,j}(q,\omega)|} \simeq \frac{V^{cc}_{j,n}}{(1-L^1\chi_{11}-L^2\chi_{11}-L^3\chi_{11}\cdots)} \ . \tag{39}$$

The function in the denominator is shown in Fig. 4 for a system in thermal equilibrium at the temperature of 100 K and with a carrier density of $1.6\times10^6$ cm$^{-1}$. The oscillations for very small wave vectors along the energy axis are due to the intersubband plasmons. Plasmon modes (i.e., zeros of the function) start to appear only at the relatively low temperature of 100 K and are usually completely Landau damped when the distribution function is strongly out of equilibrium.

In order to observe a very peculiar aspect of screening in quantum wires, we now evaluate the Lindhart expression

(37) for two extreme limits. If we consider a Maxwell Boltzmann distribution, and moreover we take the long-wavelength approximation $(q \to 0)$ and neglect the imaginary part, the expression can be computed analytically:

$$L_i(q,0) = \sum_k \frac{f[E_i(k+q)] - f(E_i(k))}{E_i(k+q) - E_i(k)} = \frac{L}{2\pi} \int_{-\infty}^{\infty} \frac{\partial f}{\partial E} \, dk$$

$$= \frac{L}{2\pi} \int_{-\infty}^{\infty} \frac{\partial f}{\partial k} \frac{1}{\partial E/\partial k} \, dk = \frac{L}{2\pi} \left[ \frac{n_i^2 \hbar^2 2\pi}{L^2 m^* K_B T} \right]^{1/2} \int_{-\infty}^{\infty} -\frac{e^{-\hbar^2 k^2/2m^* K_B T}}{K_B T} \, dk = -\frac{n_i}{K_B T} \, , \tag{40}$$

where $n_i$ is the carrier density in subband $i$. If we compare this expression to the equivalent one for 2D and 3D systems, this condition could be defined as Debye screening, which consist in a screening function always positive definite that reduces the strength of the bare CC interaction.

Let us now consider a nonequilibrium condition, where the distribution function is given by two Gaussians centered at $-\tilde{k}$ and $\tilde{k}$ and with a width characterized by $E_w$. This is a schematic representation of the system during the laser excitation. In this case, the Lindhart expression is (see Appendix B)

$$L_i(q,0) = -\frac{n_i}{E_w} + \frac{2LB_C \tilde{k}}{\pi E_w} e^{-\hbar^2 \tilde{k}^2/2m^* E_w}$$

$$\times \int_0^\infty e^{-\hbar^2 k^2/2m^* E_w} \frac{\sinh(\hbar^2 k \tilde{k}/m^* E_w)}{k} \, dk \ . \tag{41}$$

The last integral can be easily performed numerically and it is always positive. In a large range of width energy $E_w$ and injection wave vector $\tilde{k}$, its values is higher than the first negative term, so the Lindhard expression is positive and the determinant of the dielectric function for small values of $q$ (i.e., where the term $\chi_{11}$ is indefinitely large) is always negative. For large values of $q$, the determinant of the dielectric function always goes to 1 because $\chi_{11} \to 0$,

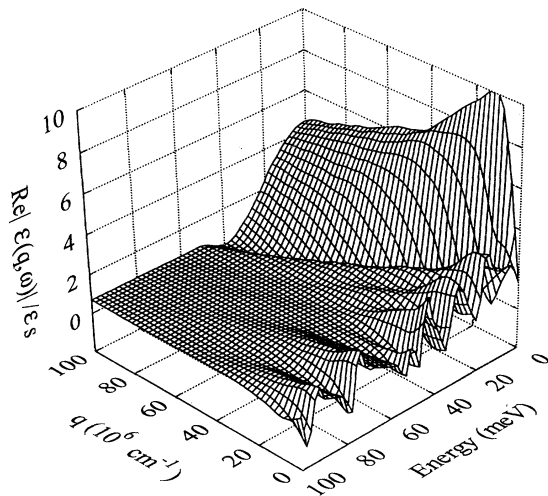and so there is always a point $q$ where the determinant is zero and the CC scattering rate is divergent. Moreover, there is an entire region where the square of the dielectric function is smaller than 1 and this results in an increase in the strength of the bare Coulomb interaction, situation often referred as antiscreening. As we will see in our results, this condition is actually met during a photoexcitation experiment and plays a major role in the thermalization process. The long-wavelength approximation can be easily dropped computing the Lindhart expression numerically as we do in our simulation but, as we will see from our results, the effect remains the same. In the present treatment, we neglected the imaginary part of the dielectric function, which contains information on the damping of the interaction. The introduction of this part is quite useful in the MC simulation, because it reduces the divergency in the CC scattering rate to a broadened peak whose height is[7]

$$W_{i,m}^{cc2} = \left[ \frac{V_{j,n}^{cc}}{\text{Im}(\varepsilon_{i,j}(q,\omega))} \right]^2 . \tag{42}$$

## III. MONTE CARLO PROCEDURE

Among the several methods used to solve the Boltzmann equation introduced in Sec. II D, the Monte Carlo approach has been intensively used in the past few years. This wide diffusion is due both to its simplicity and easy physical interpretation and to the possibility to include all kinds of scattering processes and nonlinear phenomena. The MC simulation is often regarded as a simple classical simulation of pointlike particles, but it can be shown that it corresponds to a Monte Carlo solution (from its mathematical point of view) of the Boltzmann transport equation.[17] However, if compared to a direct solution, a Monte Carlo simulation provides additional information such as, for example, noise and fluctuation properties of the system that are not contained in the Boltzmann equation.

In the present paper, we focus our attention on the electron cooling neglecting the holes for the following reasons: (i) recent ultrafast experiments[36] have shown that holes are completely thermalized within the time scale of the laser pulse, due to the much smaller excitation energy and the larger coupling with both LO and TO phonons; (ii) due to the much smaller energy separation of the levels and the relatively large broadening created by wire inhomogeneities, the valence band can be assumed as almost continuous for what concerns carrier cooling. This makes our calculation simpler, because due



FIG. 4. Determinant of the dielectric function for a system with a density of $1.6 \times 10^6$ cm$^{-1}$ in equilibrium at the temperature of 100 K.

to band mixing the valence band is not yet well known in quantum wires and the effective-mass approximation may be questionable.

Since the optical-phonon dispersion is very flat in the region where such phonons couple with electrons, we assume a constant value for the phonon energy $\hbar\omega_{\lambda,q_x} \rightarrow \hbar\omega_0$. The nonequilibrium phonon population is collected on a three-dimensional (3D) mesh. At every carrier-phonon scattering, the wave vectors $q_x$, $q_z$ and the confined phonon index $\nu$ along the $y$ direction are evaluated. For each scattering, the contribution to the phonon population (positive for emission processes, negative for absorption ones) is

$$W_\nu^{\mathrm{ph}} = \frac{8\pi^3}{V} \frac{1}{\Delta \mathbf{q}} \frac{4\pi^2}{L_x L_z} \frac{1}{\Delta q_x \Delta q_z} , \qquad (43)$$

where $\Delta q_x$ and $\Delta q_z$ are the sizes of the mesh used to collect the phonon distribution (uniform in our case). A rejection technique is used to account for the hot-phonon effects on the carrier cooling.[4] At the beginning of the simulation, a maximum value for the phonon distribution $N_M$ must be guessed and the scattering rate is computed assuming this value. Whenever during the simulation a phonon scattering is selected, the electron final state and the corresponding mode and wave vector are computed. A random number is then generated between zero and $N_M$ or $N_M + 1$ (depending if it is an absorption or emission process) and this number is compared, respectively, with $n_{\lambda,q_x}$ or $n_{\lambda,q_x} + 1$; if it is lower, the scattering process is performed and the electron and phonon distributions updated; otherwise, the process is rejected. For the decay of the hot-phonon population, we have assumed a bulk decay time of 7 ps, because at the moment there is no clear evidence that this time should be different in low-dimensional systems.

The CC scattering rate is a time-dependent rate too and a similar method is used in the MC. The Lindhart expression (37) and the maximum of the CC scattering rate are evaluated every 100 fs during the simulation using the actual Monte Carlo distribution function. The CC scattering are generated using the maximum of the rate and then an internal rejection technique is used to perform only the "real" scattering events.[38] Every time a particle undergoes a CC scattering process, a partner particle is selected, the actual rate for this pair is computed, and a random number is generated between zero and the maximum of the CC rate. If this number is smaller than the computed rate, the scattering is performed and the states of both particles updated, otherwise the scattering is rejected. In such a two-particle process, we scatter two carrier at the same time (the partner carrier being taken from the simulated ensemble); Therefore, all the CC rates used in the simulation are obtained dividing by two the single-particle ones.

In order to account for the Pauli exclusion principle, we use a similar rejection procedure. As we have seen in the previous sections, by neglecting the filling factor $(1 - f)$ in the calculation of the scattering rates, we have overestimated them. After each scattering, the value of the distribution function is evaluated, a random number

between zero and one is generated, and only if this number is smaller than $(1 - f)$ the scattering is performed. For the CC processes, this procedure must be repeated for the final state of both particles.

## IV. APPLICATIONS

One of the important advantages that the MC method offers is its ability to investigate separately the effect of the different scattering mechanisms. This is particularly useful when several nonlinear phenomena are present, because we can first understand their individual effect and then, through a complete simulation, we can verify what can be observed in a real experiment. We will then start by investigation the CC interaction and the screening effect neglecting entirely the phonon interactions. In this condition there is no energy dissipation and the injection energy has to be kept low (43 meV in the first subband), otherwise a significant fraction of the carriers would escape out of the confinement region.

Successively we add the carrier-phonon interaction and we study the joint carrier-phonon relaxation following a 100-fs laser pulse with a central energy of 1.76 eV (corresponding to a maximum excess energy of 172 meV for electrons in the first subband). We investigate the hot-phonon and degeneracy effects and we compare our results to an equivalent 3D scenario. Since all the nonlinear phenomena discussed above are density dependent, if we want to compare the cooling rates of the wire with those of the bulk, it is crucial to work with equivalent densities. We can think of at least two different approaches. The first one relates the 1D and 3D densities by taking the same number of carriers per 3D unit volume for the two systems, the second one takes densities which correspond to the same quasi-Fermi level. In the first case, we do not consider the quantized nature of the wire, because the comparison does not depend on the subband positions nor on the 1D density of states. This is certainly a good method to compare hot-phonon effects, as their effect is proportional to the volume of lattice "heated" by the electrons. In the second case, the real quantum nature of the wire is accounted for and consequently this is an appropriate method if we want to compare carrier-carrier and degeneracy effects, which are strongly dependent on the density of states.

In general, these two approaches are not equivalent over the whole density range. However, even though the two methods scale with density in a different way, for relatively high densities they result to be quite close to each other. In particular, there is a given 1D density, in our case $6.6 \times 10^6$ cm$^{-1}$, for which both methods correspond to the same 3D density of $2.2 \times 10^{18}$ cm$^{-3}$ in the bulk. We have then chosen to compare the two systems at this relatively high density and also at a very low one ($n = 10^4$ cm$^{-1}$ in the wire and $n = 3.3 \times 10^{15}$ cm$^{-3}$ in the bulk). For these low-density values, although there is no unique correspondence between the 1D and 3D densities, all the density-dependent phenomena such as hot-phonon and degeneracy effects are negligible. All the simulations are performed at the lattice temperature of 10 K.

## A. Carrier-carrier effects

At the lower excitation energy, only the first three wire subbands are directly excited. To understand the separate effect of the intrasubband and intersubband CC scattering, we initially perform three simulations at different densities including only the intrasubband mechanism. The population in each subband remains then constant after the end of the excitation, but there is an energy redistribution between the different subbands. We can notice the two main effects of the intrasubband interaction: Fig. 5(a) shows the total distribution function plotted as a function of the wave vector for an excitation density of $10^5$ cm$^{-1}$. After the end of the excitation, there is no change in the distribution and the curves at $t = 0.4$ and $2.0$ ps overlap perfectly. If we look at the separate subband populations Figs. 5(b), 5(c), and 5(d), we can see that carriers are injected at $k_x = 2.8$, $2.2$, and $0.5 \times 10^6$ cm$^{-1}$ in the three subbands, but already at $t = 0.4$ ps in each subband there is a replica of the excitation peaks injected in the other subbands. This is the effect described in Sec. II D 2, in which two carriers simply swap their initial momentum, the kinetic energy in each subband is equilibrated, but there is no change in

the total distribution function (as a function of the wave vector), because the total number of particles for a given value of $k_x$ remains the same. Figures 6 and 7 show the same effect, but at the higher densities of $5 \times 10^5$ cm$^{-1}$ and $10^6$ cm$^{-1}$. Looking at the time evolution of the subband distribution functions, we notice that the strength of the interaction increases going from $10^5$ to $5 \times 10^5$ cm$^{-1}$, but levels off afterwards.

Figures 8, 9, and 10 show the corresponding results when the intersubband CC interaction is also included. In addition to the transfer of energy from one subband to the other, now there is a significant scattering of particles. When a particle scatters in a different subband, the final wave vector of both particles is different from the initial one because the subband energy difference enters the energy conserving delta. Already at a density of $10^5$ cm$^{-1}$, Fig. 8, we can observe a strong broadening of the initial excitation peaks, both in the separate subband distribution, as well as in the total one. Nevertheless we can still notice at $t = 0.4$ ps the replicas created by the intrasubband scattering. This means that intrasubband processes are stronger than intersubband ones even though they are less effective in thermalizing the distribution. This result allows us to state that *CC interaction must always be considered in multisubband quantum*
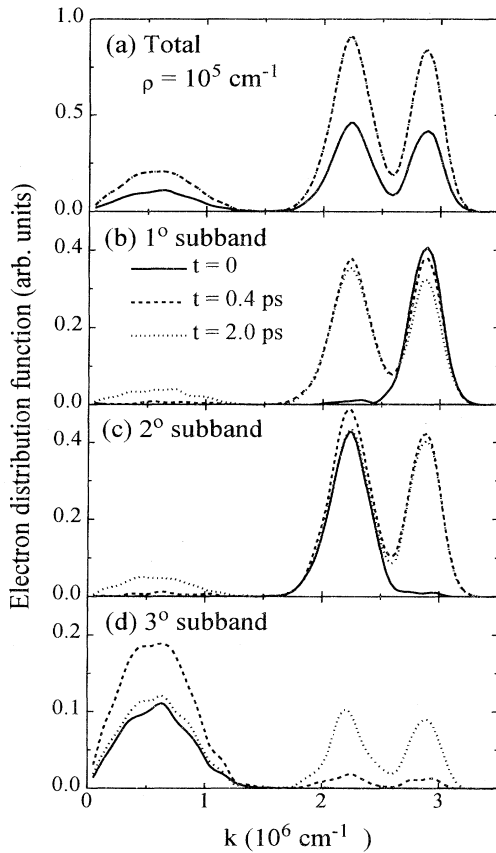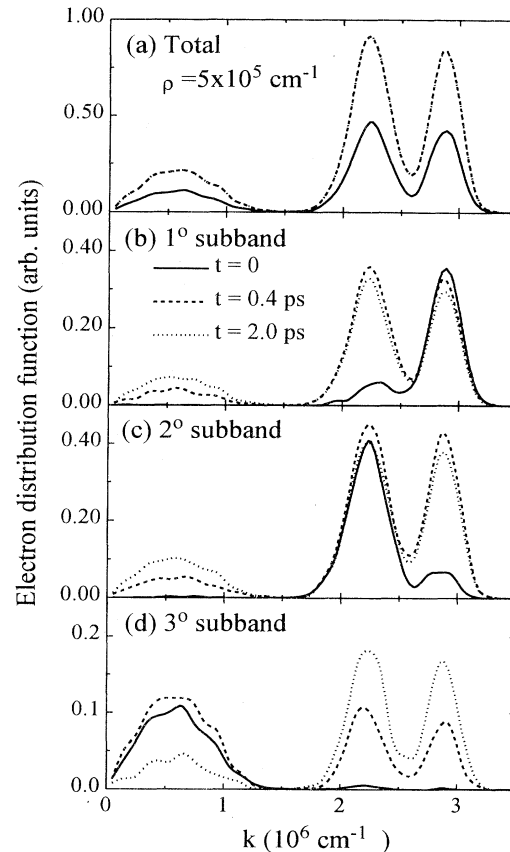
FIG. 5. Electron distribution function as a function of the electron wave vector: (a) total and (b), (c), and (d) in the first three subbands for an electron density of $10^5$ cm$^{-1}$, when only the intrasubband CC scattering mechanism is present.

FIG. 6. Electron distribution function as a function of the electron wave vector: (a) total and (b), (c), and (d) in the first three subbands for an electron density of $5 \times 10^5$ cm$^{-1}$, when only the intrasubband CC scattering mechanism is present.

*wires, even for relatively low carrier densities.* Figures 9 and 10 show the same effect at higher carrier densities. Now the effect of the intersubband CC is much stronger and the intrasubband replicas almost disappeared. Moreover, we can see that in this case, the interaction is even stronger at $5 \times 10^5$ cm$^{-1}$ than at $10^6$ cm$^{-1}$. This effect is due to the fact that, at different densities, the zero in the real part of the dielectric function (i.e., the divergency in the scattering rate) during the nonequilibrium transient moves at different values of $q$ and in doing so, it can enhance the scattering rate in a region more populated by particles, thus making it possible to have a higher effective rate at a lower density.

Figures 11 and 12 show the time evolution of the kinetic energy in the first three subbands for the respective densities of $10^5$ and $5 \times 10^5$ cm$^{-1}$. The upper part of each figure shows the result of the simulations performed with only the intrasubband CC scattering. At the lower density the thermalization takes quite a long time, in particular for the third subband that even after 2 ps has an average kinetic energy different from the other two subbands. When the intersubband CC is included, the process becomes much faster, Fig. 11(b), and already after 0.6 ps the three subbands have equilibrated to the same energy.

For the higher density of $5 \times 10^5$ cm$^{-1}$, Fig. 12, both processes become faster and the kinetic energy of all subbands becomes equal after 300 fs only. Even in this case, the interaction does not show any increase with increasing density. The oscillatory and step behavior in both figures is due to the rapid change in the dielectric function during the carrier relaxation and this suggests that a shorter time step in the update of the screening function could result in a slightly smoother evolution, although it would not change the main result.

To understand the peculiar density dependence shown by the previous results, in particular the negligible density dependence of the interaction above $5 \times 10^5$ cm$^{-1}$, we need to consider the time evolution of the screening function. In Fig. 13, we have plotted the determinant of the real part of the dielectric function (left-hand side) and of the CC scattering rate (right-hand side) for a simulation performed with an injection density of $10^6$ cm$^{-1}$ at four different times. Due to the combined effect of the changes in electron distribution function (shown in the inset) and in screening, the CC scattering rate can have sensible variation in a relatively short time. At $t = 0$ and 1.2 ps, we can see that the strong nonequilibrium distribution results in a negative dielectric function for small
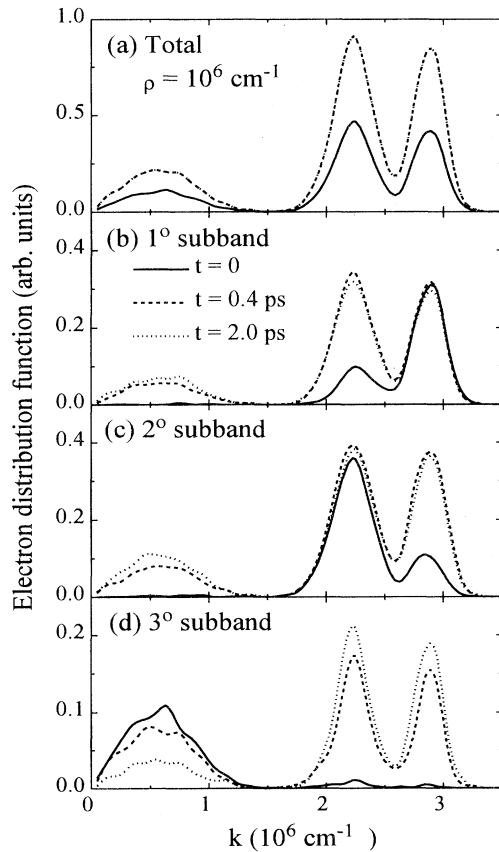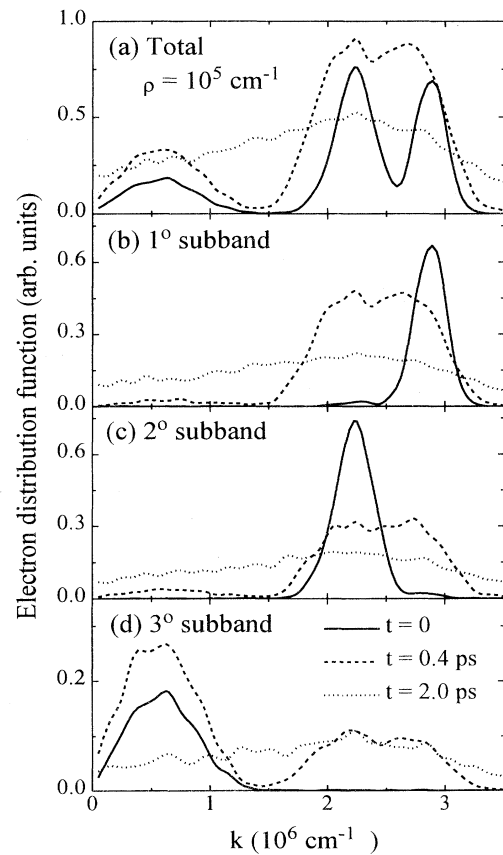


FIG. 7. Electron distribution function as a function of the electron wave vector: (a) total and (b), (c), and (d) in the first three subbands for an electron density of $10^6$ cm$^{-1}$, when only the intrasubband CC scattering mechanism is present.



FIG. 8. Electron distribution function as a function of the electron wave vector: (a) total and (b), (c), and (d) in the first three subbands for an electron density of $10^5$ cm$^{-1}$ when both intrasubband and intersubband CC scattering mechanism are present.

values of $q_x$; in turn the zero in the dielectric function (shown by the crossing of the dashed line) results in a very high scattering rate for CC interaction. Here, the solid line is the sum of the intrasubband and intersubband rate, while the dashed line represents only the contribution of the intersubband rate. Although the intrasubband rate is much larger in this regime, we can see that the intersubband rate is in the range of 10–100 scattering per picosecond, i.e., much stronger that the carrier-phonon scattering rate. At later times, the dielectric function becomes again completely positive and the antiscreening effects disappear; correspondingly both the intrasubband and intersubband scattering rates diminish strongly. At $t = 7.6$ ps, we have plotted for comparison the dielectric function that results from a Maxwell-Boltzmann equilibrium distribution (dotted line). As our QWR system is degenerate, we can see the actual dielectric function is much lower, i.e., the screening is much weaker than predicted by a simple nondegenerate Debye model. At sufficiently low density, the screening function is never very different from $\varepsilon_s$ and cannot become negative, except for a very small value of the wave vector $q_x$ (too small values of the wave-vector exchanged in a CC scattering do not affect significantly the distribution function). When the density is increased, the minimum of the dielectric function (i.e., the point at $q_x = 0$) moves towards larger negative values and correspondingly the zero moves to larger values of $q_x$, making the interaction more effective. A further increase of the density only results in a small change in the position of this zero and so does not affect significantly the scattering rate.

## B. Hot-phonon effects

We now focus on carrier relaxation when the interaction of carriers with phonons is also included, together with the CC interaction. In Figs. 14(a) and 14(b), we show the density dependence of the cooling, respectively, in quantum wires and bulk. The solid line corresponds to a sufficiently low density for the cooling to proceed through a simple cascade of phonon emission processes: the phonon population is not driven out of equilibrium and degeneracy effects are completely negligible. The highest densities, respectively $6.6 \times 10^6$ cm$^{-1}$ in the wire and $2.2 \times 10^{18}$ cm$^{-3}$ in the bulk, have been chosen as explained in Sec. IV in order to have comparable degenera-
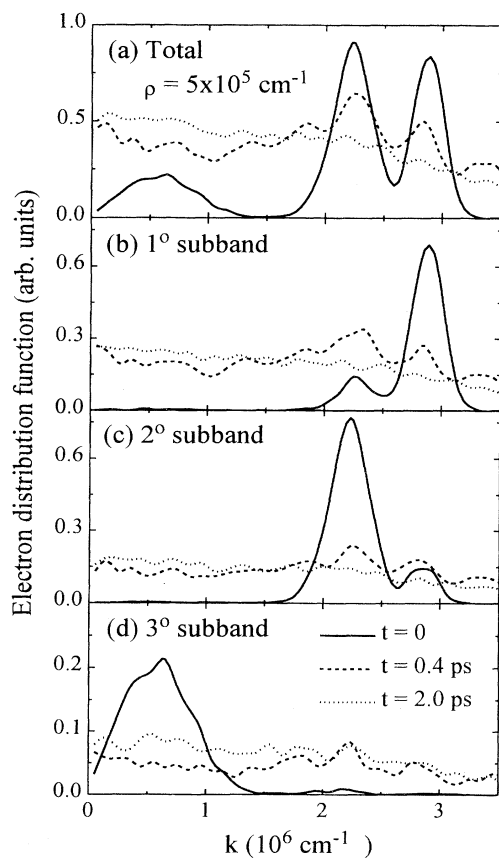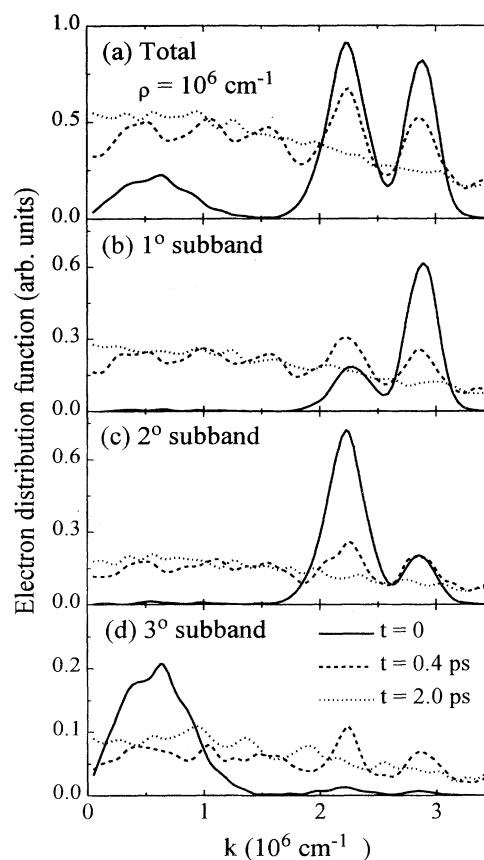


FIG. 9. Electron distribution function as a function of the electron wave vector: (a) total and (b), (c), and (d) in the first three subbands for an electron density of $5 \times 10^5$ cm$^{-1}$, when both intrasubband and intersubband CC scattering mechanism are present.



FIG. 10. Electron distribution function as a function of the electron wave vector: (a) total and (b), (c), and (d) in the first three subbands for an electron density of $10^6$ cm$^{-1}$, when both intrasubband and intersubband CC scattering mechanism are present.
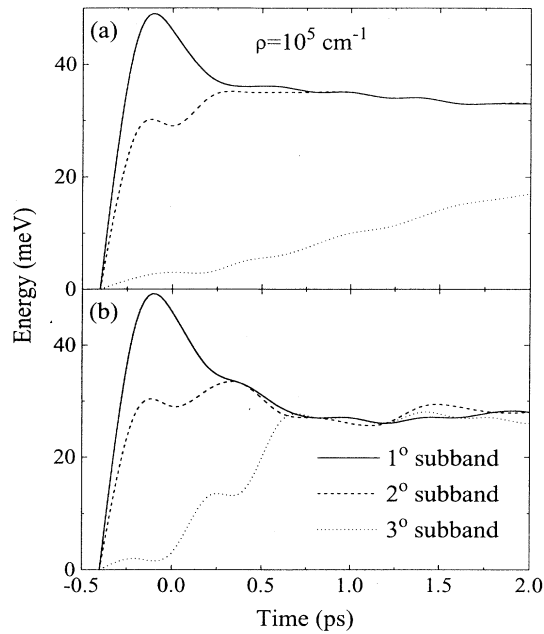
FIG. 11. Time evolution of the kinetic energy in the first three subbands for the density of $10^5$ cm$^{-1}$, (a) only intrasubband carrier-carrier scattering included, (b) both intrasubband and intersubband scattering.
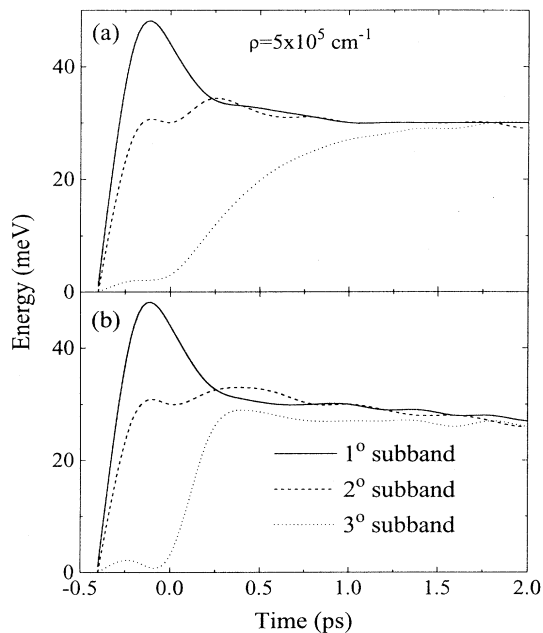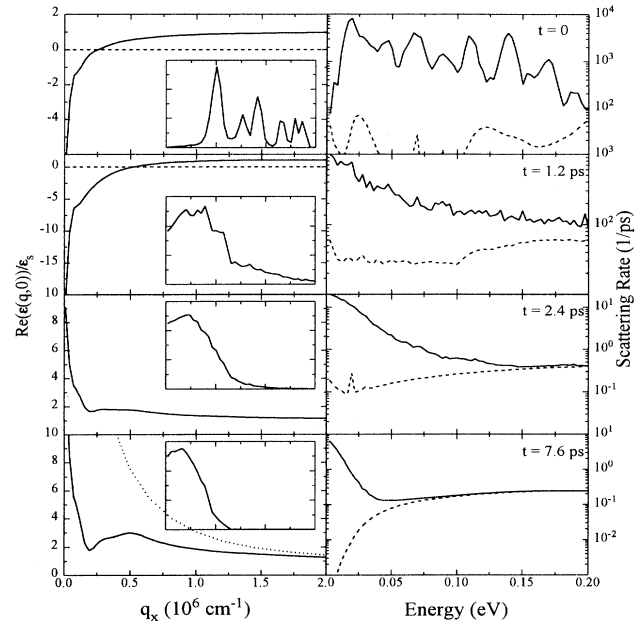


FIG. 13. Time evolution of the screening function used in the Monte Carlo (left-hand side) and of the corresponding CC scattering rate (right-hand side). The insets show schematically the electron distribution as a function of energy, see text for details.

cy and hot-phonon effects. Let us consider the spread in energy between the lowest- and highest-density cases: clearly, the density dependence in the wire is less pronounced than in bulk. This can be seen more clearly in Fig. 15, where the extreme cases for wire and bulk have been plotted together.

As found previously,[39] at low density the cooling in the wire (solid line) is slower than in the bulk (dashed line),



FIG. 12. Time evolution of the kinetic energy in the first three subbands for the density of $5 \times 10^5$ cm$^{-1}$, (a) only intrasubband carrier-carrier scattering included, (b) both intrasubband and intersubband scattering.
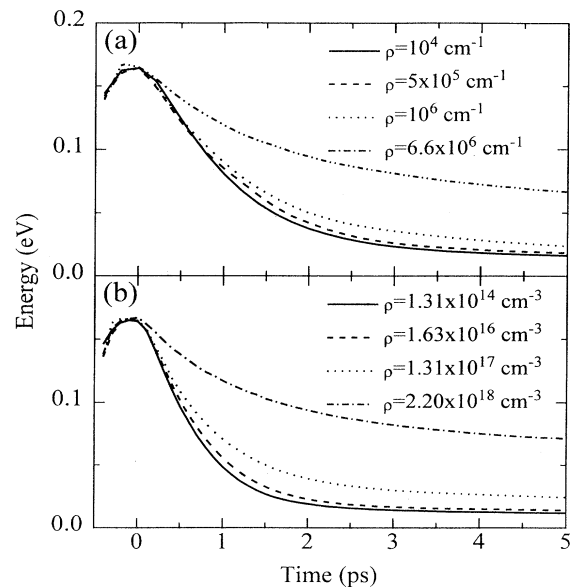


FIG. 14. Carrier cooling as a function of the injection density in the quantum wire (a) and bulk (b).
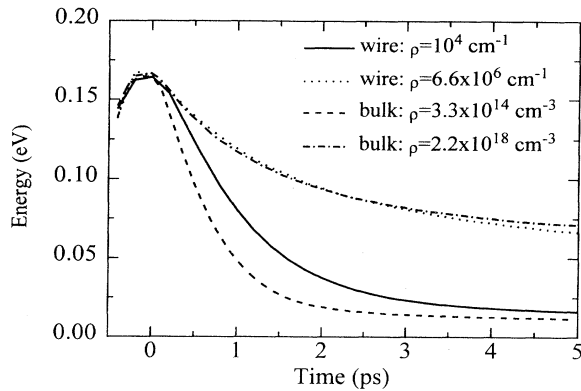
FIG. 15. Comparison between the carrier cooling in quantum wires and bulk at high and low carrier density.

due to the reduced efficiency of the intersubband phonon scattering. At higher densities (dotted and dash-dotted line, respectively, for the wire and the bulk), the almost perfect overlap of the two curves is quite remarkable; this is mainly due to a reduced phonon reabsorption in the wire and to a reduction of the intersubband phonon scattering due to phase-space filling compared to the bulk case.

Finally, in order to compare the two nonlinear effects, we performed additional simulations, considering separately degeneracy and hot-phonon effects. The result is shown in Figs. 16(a) and 16(b), respectively, for the wire and the bulk. Both effects contribute approximately in the same way to the reduction of the cooling. The only appreciable difference in the two systems is that at relatively short time, about 1 ps, the effect of degeneracy alone is much weaker in bulk than in the wire. This is
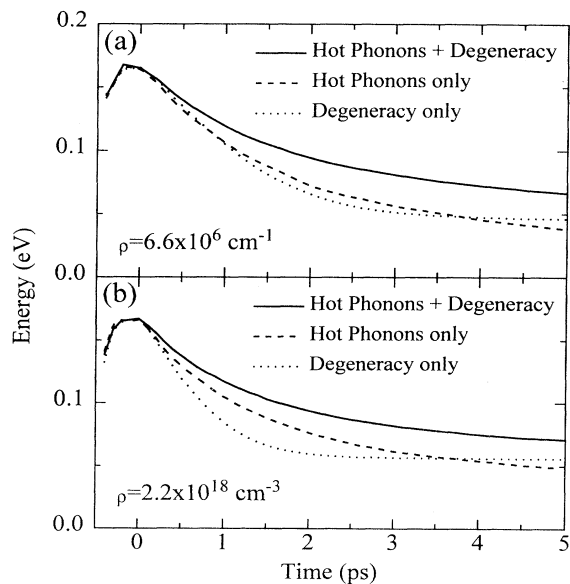


FIG. 16. Carrier cooling when degeneracy and hot-phonon effects are included separately in the quantum wire (a) and bulk (b).

due to the fact that, at short times, the cooling in bulk systems is not slowed down by degeneracy effects, since electrons need to emit several phonons before entering the region in which band filling becomes important. On the contrary, in the wire, degeneracy is more important even at shorter times and higher-energy states, because band filling is present in each subband separately, and due to the reduced intersubband rate, even relatively high-energy subbands can become degenerate immediately after the laser excitation.

To conclude our analysis, we now investigate the time evolution of the phonon distribution functions. Within our model, due to the symmetry of the electron wave functions and the phonon potentials, well-defined scattering selection rules exist, based on the parity of the initial and final states. In particular, phonon modes with even potential contribute only to intrasubband transitions and to transitions between subbands for which the $y$ index difference is even, whereas odd modes contribute to scattering between subbands with odd index difference. One important difference between 1D and 3D systems is that in bulk materials it is not possible to emit phonons with a very small wave vector ( $\leq 10^5$ cm$^{-1}$), due to energy and momentum conservation. The same arises in quantum wires for intrasubband scattering. However, when the subband spacing is close to the energy of the optical phonon, intersubband scattering processes can occur with the emission or absorption of a phonon with wave vector $q_x$ close to zero.[39] This fact could have important consequences for light-scattering experiments. Indeed, Raman study of hot phonons in quantum wells has always been difficult due to the very small *in plane* wave vector probed in off-resonance backscattering experiments. The presence of very small wave-vector hot phonons could allow a detailed Raman investigation of the process of carrier and phonon cooling. The different confined phonon modes are heated in a different way. In Fig. 17, we plot $n_{q_x}$ for the first two phonon modes as a function of $q_x$ at four different times and for a fixed $q_z = 2 \times 10^5$ cm$^{-1}$. The choice of such a small $q_z$ value allows us to focus mainly on intersubband transitions involving only $y$ subbands, which for this type of wires should be the most interesting ones as most of the intersubband dynamics involve scattering within the same $z$ subband. Figure 17(a) corresponds to the first even mode and shows a series of peaks corresponding to wave vectors of phonons involved in preferred intrasubband phonon emissions in the different subbands. These peaks are related to the energy position of the initial excitation in each subband. The first small peak corresponds instead to intersubband phonon scattering between nonadjacent subbands, in particular from subband 3 to 1. The amplitude of this peak is quite small because, due to the small form factor, few electrons undergo this transition. The diamonds represent the hot-phonon distribution of the corresponding bulk simulations for $t = 0.4$ ps; as we can see, both the shape and the amplitude are quite similar.

The most interesting feature can be observed in the second-phonon mode (odd one) shown in Fig. 17(b), where we clearly observe the emission of phonons with very small wave vectors. There are several different ener-
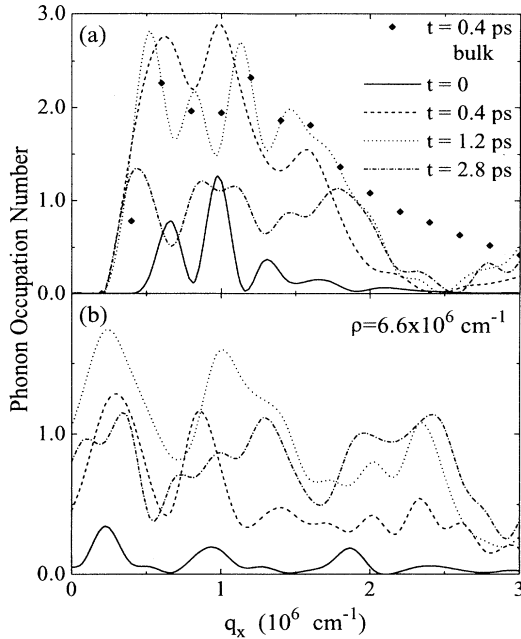
FIG. 17. Evolution of the phonon distribution function after the laser excitation: (a) first and (b) second $y$ phonon mode. The diamonds in part (a) correspond to the hot-phonon distribution in the bulk following the equivalent excitation condition.

## V. CONCLUSIONS

We have presented a Monte Carlo investigation of carrier relaxation in quasi-one-dimensional systems. The strength of the carrier-carrier interaction and the screening effects have been studied as a function of density. Our results show that in multisubband quantum wires, this interaction is very important even at relatively low densities and that the density dependence of the interaction is not as strong as in 2D and 3D systems. The difference between the present results and that of our previous investigation[11] is due to an improvement in the screening model, obtained by dropping the long-wavelength approximation. The magnitude of this difference suggests that a fully dynamical-screening calculation might show further interesting effects.

The results concerning carrier cooling and relaxation demonstrate that, for the relatively large wires made available by the current technology, the general trend is similar to the bulk one. Nevertheless, the hot-phonon population contains much information about the dynamical process following laser excitation, as well as on the structure of the wire. We have shown that the dynamics of phonon populations in wires takes place in a wave-vector range, which is accessible to off-resonance time-resolved Raman experiments: this possibility—which does not exist for bulk and is not normally available in quantum well structures—should open the way to a direct experimental investigation of the joint evolution of carrier and phonon distributions.

## APPENDIX A

The expression for the dielectric matrix in the diagonal approximation (38) can be further simplified, if we consider that all intrasubband form factors are very close to each other, because they contain only the squared wave functions. We can then write

$$
\varepsilon_{i,j}(q,\omega) = \begin{vmatrix} 1-L^1\chi_{11} & -L^2\chi_{11} & -L^3\chi_{11} & \cdots \\ -L^1\chi_{11} & 1-L^2\chi_{11} & -L^3\chi_{11} & \cdots \\ -L_1\chi_{11} & -L^2\chi_{11} & 1-L^3\chi_{11} & \cdots \\ \vdots & \vdots & \vdots & \ddots \end{vmatrix}.
$$

(A1)

This matrix can be written symbolically as

$$\mathbf{E} = \mathbf{I} - \mathbf{C} \cdot \mathbf{R} ,$$    (A2)

where $\mathbf{I}$ is the identity matrix, while $\mathbf{C}$ and $\mathbf{R}$ are the row and column vectors:

gy splittings between adjacent subbands, which lead to a series of preferred wave vectors corresponding to the various structures visible in the figure. We also notice two additional features: in Fig. 17(a), the phonon population reaches its maximum after only 400 fs, while for the odd mode, Fig. 17(b), the maximum is reached only after 1 ps. Since the intrasubband scattering rate is higher than the intersubband one, electrons tend to first cool within their subband, emitting even mode phonons, transferring then into lower subbands only at later times.[10,11] For the same reason, also hot-phonon reabsorption is delayed for the odd modes and is less effective. In fact, in the quantum wire, as in higher-dimensionality systems, hot-phonon reabsorption is important only at small wave vectors as can be seen in Figs. 17(a) and 17(b) by looking at the curve corresponding to $t = 2.8$ ps. Due to some relatively large subband spacing, a lot of intersubband phonons are emitted with a large wave vector and cannot be reabsorbed anymore.

It is important to notice that hot phonons can have a different effect if the CC interaction is not included.[13] In this case, the excited carrier population relaxes only through a phonon-cascade emission and the hot-phonon population increases only in a very limited region of the phase space. However, for a realistic case, even in the presence of very narrow excitations, we have seen that the CC interaction spreads out the carriers on a broad energy range. This in turn results in a buildup of the phonon population at all wave vectors as we have just seen.

$$\mathbf{C} = (111 \cdots); \quad \mathbf{R} = \begin{bmatrix} L^1\chi_{11} \\ L^2\chi_{11} \\ L^3\chi_{11} \\ \vdots \end{bmatrix}. \tag{A3}$$

In this case, it can be shown[40] that the inverse matrix is

$$\mathbf{E}^{-1} = \mathbf{I} + \lambda \mathbf{C} \cdot \mathbf{R}, \tag{A4}$$

where

$$\lambda = \frac{1}{1 - \mathbf{R} \cdot \mathbf{C}} = \frac{1}{1 - L^1\chi_{11} - L^2\chi_{11} - L^3\chi_{11} - \cdots} = \frac{1}{|\mathbf{E}|}. \tag{A5}$$

After simple rearrangements, we can finally write

$$\varepsilon_{m,n}^{-1} = \frac{1}{|\mathbf{E}|} \begin{bmatrix} 1 - \sum_{n, n \neq 1} L^n\chi_{11} & L^2\chi_{11} & L^3\chi_{11} & \cdots \\ L^1\chi_{11} & 1 - \sum_{n, n \neq 2} L^n\chi_{11} & L^3\chi_{11} & \cdots \\ L^1\chi_{11} & L^2\chi_{11} & 1 - \sum_{n, n \neq 3} L^n\chi_{11} & \cdots \\ \vdots & \vdots & \vdots & \ddots \end{bmatrix}. \tag{A6}$$

Now we can compute the total potential; for example, for an electron in subband 1, we have

$$W_{11}^{cc}(q) = \frac{V_{11}^{cc}(q)}{|\mathbf{E}|} + \frac{\chi_{11}}{|\mathbf{E}|} \sum_{n, n \neq 1} L^n [V_{nn}^{cc}(q) - V_{11}^{cc}(q)]. \tag{A7}$$

Once again, as the different intrasubband matrix elements are very close to each other, as a first approximation, we can keep only the first term and we have then obtained Eq. (39).

## APPENDIX B

Let us evaluate the Lindhart expression when the electron distribution function is given by

$$f_i(k) = \frac{1}{2} \left[ \frac{n_i^2 \hbar^2 2\pi}{L^2 m^* E_w} \right]^{1/2} \{ e^{-\hbar^2(k-\bar{k})^2/2m^* E_w} + e^{-\hbar^2(k+\bar{k})^2/2m^* E_w} \} = B_C \{ e^{-\hbar^2(k-\bar{k})^2/2m^* E_w} + e^{-\hbar^2(k+\bar{k})^2/2m^* E_w} \}.$$

We have

$$L^i(q,0) = -\frac{LB_C}{2\pi} \frac{1}{E_w} \left\{ \int_{-\infty}^{\infty} \frac{k-\bar{k}}{k} e^{-\hbar^2(k-\bar{k})^2/2m^* E_w} dk + \int_{-\infty}^{\infty} \frac{k+\bar{k}}{k} e^{-\hbar^2(k+\bar{k})^2/2m^* E_w} dk \right\}$$

$$= -\frac{LB_C}{2\pi} \frac{1}{E_w} \left\{ \int_{-\infty}^{\infty} e^{-\hbar^2(k-\bar{k})^2/2m^* E_w} dk - \int_{-\infty}^{\infty} \frac{\bar{k}}{k} e^{-\hbar^2(k-\bar{k})^2/2m^* E_w} dk + \int_{-\infty}^{\infty} e^{-\hbar^2(k+\bar{k})^2/2m^* E_w} dk \right.$$

$$\left. + \int_{-\infty}^{\infty} \frac{\bar{k}}{k} e^{-\hbar^2(k+\bar{k})^2/2m^* E_w} dk \right\}$$

$$= -\frac{n_i}{2E_w} + \frac{LB_C \bar{k}}{2\pi E_w} e^{-\hbar^2\bar{k}^2/2m^* E_w} \left\{ \int_0^{\infty} e^{-\hbar^2 k^2/2m^* E_w} \frac{e^{\hbar^2 k\bar{k}/m^* E_w}}{k} dk + \int_{-\infty}^0 e^{-\hbar^2 k^2/2m^* E_w} \frac{e^{\hbar^2 k\bar{k}/m^* E_w}}{k} dk \right\}$$

$$- \frac{n_i}{2E_w} - \frac{LB_C \bar{k}}{2\pi E_w} e^{-\hbar^2\bar{k}^2/2m^* E_w} \left\{ \int_0^{\infty} e^{-\hbar^2 k^2/2m^* E_w} \frac{e^{-\hbar^2 k\bar{k}/m^* E_w}}{k} dk + \int_{-\infty}^0 e^{-\hbar^2 k^2/2m^* E_w} \frac{e^{-\hbar^2 k\bar{k}/m^* E_w}}{k} dk \right\}$$

$$= -\frac{n_i}{E_w} + \frac{2LB_C \bar{k}}{\pi E_w} e^{-\hbar^2\bar{k}^2/2m^* E_w} \int_0^{\infty} e^{-\hbar^2 k^2/2m^* E_w} \frac{\sinh(\hbar^2 k \frac{\bar{k}}{m^*} E_w)}{k} dk.$$

[1] See, e.g., C. Weisbuch and B. Vinter, *Quantum Semiconductor Structures. Fundamentals and Applications* (Academic, Boston, 1991); in *Nanostructure Physics and Fabrication*, edited by M. A. Reed and P. Kirk (Academic, Boston, 1989).

[2] H. Sakaki, Jpn. J. Appl. Phys. **19**, L735 (1980); **28**, L314 (1989).

[3] See, e.g., the volume, *Hot Carriers in Semiconductor Nanostructures: Physics and Applications*, edited by J. Shah (Academic, Boston, 1992).

[4]P. Lugli, P. Bordone, L. Reggiani, M. Rieger, P. Kocevar, and S. M. Goodnick, Phys. Rev. B **39**, 7852 (1989), and references therein.

[5]V. B. Campos and S. Das Sarma, Phys. Rev. B **45**, 3898 (1992); V. B. Campos, S. Das Sarma, and M. A. Stroscio, *ibid.* **46**, 3849 (1992).

[6]Q. P. Li and S. Das Sarma, Phys. Rev. B **43**, 11 768 (1991).

[7]B. Y. Hu and S. Das Sarma, Phys. Rev. B **48**, 5469 (1993).

[8]Q. P. Li, S. Das Sarma, and R. Joynt, Phys. Rev. B **45**, 13 713 (1992).

[9]U. Bockelmann and G. Bastard, Phys. Rev. B **42**, 8947 (1990).

[10]P. Lugli, L. Rota, and F. Rossi, Phys. Status Solidi B **173**, 229 (1992).

[11]L. Rota, F. Rossi, S. M. Goodnick, P. Lugli, E. Molinari, and W. Porod, Phys. Rev. B **47**, 1632 (1993).

[12]K. W. Kim, M. A. Stroscio, A. Bhatt, R. Mickevicius, and V. V. Mitin, J. Appl. Phys. **70**, 319 (1991); R. Mickevicius, V. V. Mitin, K. W. Kim, M. A. Stroscio, and G. J. Iafrate, J. Phys. Condens. Matter **4**, 4959 (1992).

[13]R. Mickevičius, R. Gaška, V. Mitin, M. A. Stroscio, and G. J. Iafrate, Semicond. Sci. Technol. **9**, 889 (1994).

[14]J. P. Leburton, J. Appl. Phys. **56**, 2850 (1984); S. Briggs and J. P. Leburton, Phys. Rev. B **38**, 8163 (1988); S. Briggs, D. Jovanovic, and J. P. Leburton, Appl. Phys. Lett. **54**, 2012 (1989); D. Jovanovic, S. Briggs, and J. P. Leburton, Phys. Rev. B **42**, 11 108 (1990).

[15]R. Cingolani, H. Lage, L. Tapfer, H. Kalt, D. Heitmann, and K. Ploog, Phys. Rev. Lett. **67**, 891 (1991).

[16]For a recent review see, R. Cingolani and R. Rinaldi, Riv. Nuovo Cimento **16**, 1 (1993).

[17]F. Rossi, P. Poli, and C. Jacoboni, Semicond. Sci. Technol. **7**, 1017 (1992).

[18]C. Jacoboni and P. Lugli, *The Monte Carlo Method for Semiconductor Device Simulation* (Springer Verlag, Wien, 1989).

[19]R. Rinaldi, R. Cingolani, M. Lepore, M. Ferrara, I. M. Catalano, F. Rossi, L. Rota, E. Molinari, P. Lugli, U. Marti, D. Martin, F. Morier-Gemoud, P. Ruterana, and F. K. Reinhart, Phys. Rev. Lett. **73**, 2899 (1994).

[20]B. Jusserand and M. Cardona, in *Light Scattering in Solids V*, edited by M. Cardona and G. Güntherodt (Springer, Berlin, 1989), p. 49.

[21]J. Menéndez, J. Lumin. **44**, 285 (1989).

[22]E. Molinari, in *Confined Electrons and Photons: New Physics and Applications,* edited by C. Weisbuch (Plenum, New York, 1994).

[23]P. A. Knipp and T. L. Reinecke, Phys. Rev. B **48**, 5700 (1993).

[24]K. Huang and B. Zhu, Phys. Rev. B **38**, 13 377 (1988).

[25]H. Rücker, E. Molinari, and P. Lugli, Phys. Rev. B **45**, 6747 (1992).

[26]E. Molinari, C. Bungaro, F. Rossi, L. Rota, and P. Lugli, in *Phonons in Semiconductor Nanostructures,* edited by J. P. Leburton, J. Pascual, and C. Sotomayor Torres (Kluwer, Dordrecht, 1993), and references therein.

[27]N. Mori and T. Ando, Phys. Rev. B **40**, 6175 (1989).

[28]L. F. Register, Phys. Rev. B **45**, 8756 (1992).

[29]T. Kuhn and F. Rossi, Phys. Rev. Lett. **69**, 977 (1992); Phys. Rev. B **46**, 7496 (1992).

[30]F. Rossi, S. Haas, and T. Kuhn, Phys. Rev. Lett. **72**, 152 (1994).

[31]A. Leitenstorfer, A. Lohner, T. Elsaesser, S. Haas, F. Rossi, T. Kuhn, W. Klein, G. Boehm, G. Traenkle, and G. Weimann, Phys. Rev. Lett. **73**, 1687 (1994).

[32]J. A. Kash and J. C. Tsang, in *Light Scattering in Solids VI,* edited by M. Cardona and G. Güntherodt (Springer, Berlin, 1989), p. 423.

[33]E. D. Siggia and P. C. Kwok, Phys. Rev. B **2**, 1024 (1970).

[34]J. P. Leburton, S. Briggs, and D. Jovanovic, Superlatt. Microstruct. **8**, 209 (1990); J. P. Leburton and D. Jovanovic, Semicond. Sci. Technol. **7**, B202 (1992).

[35]M. Mosko and V. Cambel, Phys. Rev. B **50**, 8864 (1994).

[36]T. Elsaesser, J. Shah, L. Rota, and P. Lugli, Phys. Rev. Lett. **66**, 1757 (1991); L. Rota, P. Lugli, T. Elsaesser, and J. Shah, Phys. Rev. B **47**, 4226 (1991).

[37]S. M. Goodnick and P. Lugli, Phys. Rev. B **37**, 2578 (1988); **38**, 10 135 (1988).

[38]M. Mosko and A. Moskova, Phys. Rev. B **44**, 10 794 (1991).

[39]A partial account of this result was reported in L. Rota, J. F. Ryan, F. Rossi, P. Lugli, and E. Molinari, Europhys. Lett. **28**, 277 (1994).

[40]*CRC Handbook of Tables for Mathematics* (CRC, Cleveland, 1975).